Chapter 4
Devices Based on Diperfluorohexyl-quaterthiophene Derivatives

For high-brightness OLEDs, and for electrically pumped organic lasers, it is important to implement materials and device configurations that allow high electroluminescence efficiencies at high current densities. In conventional OLEDs high quantum efficiencies have been reported [38, 39, 262–265], even approaching an internal quantum efficiency of 100% [34]. However, in these devices the point of maximum η_{ext} is typically reached at low current densities (in the order of 10^{-2} A/cm^2) because of increased non-radiative losses at higher voltage bias [217, 266–268].

In ambipolar polymer light-emitting transistors on the other hand, current densities of 50 A/cm^2 could be achieved without reduction of η_{ext} ($\sim$0.75%) [67]. This current density could be further increased by using another gate-dielectric [69], although in this case a decrease of η_{ext} was observed at higher bias, which was attributed to singlet-polaron quenching. In addition, Takenobu *et al.* reported current densities of several hundreds A/cm^2 in tetracene and rubrene single-crystal light-emitting transistors [75]. Despite the absence of roll-off the η_{ext} of these single-crystal devices was, however, only on the order of 0.03%. More recently, current densities of kA/cm^2 were reported for solution processed bilayer LEOFETs having an η_{ext} of 0.15% [63].

In our OLEDs with field-effect electron transport a similar behavior has been observed. In the previous chapter (Chap. 3) we have demonstrated that in a device comprising PTAA as the hole-transporting material, Alq_3 doped with DCM_2 as the active light-emitting layer and PTCDI-$C_{13}H_{27}$ as the electron-transporting material, an electron current density of $\sim$ 5 kA/cm^2 could be achieved without significant roll-off of η_{ext}. The maximum η_{ext} of these OLEDs with field-effect-assisted electron transport was however rather low. In a device comprising a 50-nm thick PTCDI-$C_{13}H_{27}$ layer, a maximum η_{ext} of 0.02% could be achieved. This efficiency could be increased to 0.05% by reducing the PTCDI-$C_{13}H_{27}$ layer thickness, indicating that re-absorption of emitted photons by PTCDI-$C_{13}H_{27}$ is a main limitation with respect to device performance. In order to further improve device performance, other materials or material combinations should be used.

In this chapter, two alternative electron-transporting materials are investigated for use as the electron-transporting material in OLEDs with field-effect electron transport: DFH-4T [269] and DFHCO-4T [237]. Both materials were selected according

S. Schols, *Device Architecture and Materials for Organic Light-Emitting Devices*,
DOI 10.1007/978-94-007-1608-7_4, © Springer Science+Business Media B.V. 2011

to the criteria that are important in our device architecture. Before device fabrication, the absorption spectrum and the morphology of the materials are studied. This is subject of Sect. 4.1. Next, transistors as well as OLEDs with field-effect-assisted electron transport comprising DFH-4T and DFHCO-4T as the electron-transporting material are investigated. Special attention is given to the achievable η_{ext} at high current densities. In Sect. 4.2 transistors and OLEDs based on DFH-4T are discussed, whereas Sect. 4.3 focuses on the performance of devices comprising DFHCO-4T. An overview of the performance of different OLEDs with field-effect-assisted electron transport fabricated using various electron-transporting materials is given in Sect. 4.4. The results reported in this chapter have been published in two different articles [251, 270].

4.1 Characterization of the Electron-Transporting Materials DFH-4T and DFHCO-4T

The first material that has been investigated is DFH-4T, which was developed for use in electron-conducting thin-film transistors [269]. The molecular structure of DFH-4T can be found in Chap. 2 (Sect. 2.1.1). The material has a LUMO of 3.3 eV [237], which is slightly lower than the LUMO of Alq_3 (2.8 eV) [235] and DCM_2 (3.1 eV) [235]. From AFM analysis of thin DFH-4T films deposited by vacuum thermal evaporation, typical Stransky-Krastanov growth is observed [271, 272]. This implies that the growth of the first few DFH-4T monolayers is two-dimensional (2D). However, beyond a certain thickness threshold the film starts to roughen strongly and the growth becomes three-dimensional (3D). In the case of DFH-4T films, this 3D growth manifests itself in the formation of thick elongated needles. Figure 4.1(a) shows an AFM topography image of a 50-nm thick (as measured by a quartz crystal monitor) DFH-4T film grown on PTAA. At the bottom of the film the presence of terraces is clearly visible. Their step height is about 6 nm, corresponding to the length of two molecules [272]. On top of this 2D layer, 3D needles (up to 200 nm high) are observed. Figure 4.1(b) shows the AFM gradient image of the same DFH-4T layer. This is quite equivalent to the topography image shown in Fig. 4.1(a), however, the 2D areas and 3D needles can be recognized more clearly.

We found that the size of the 3D needles strongly depends on the deposition rate. Increasing the deposition flux reduced their height from ∼300 nm to ∼100 nm. The density of the 3D features could be controlled by the substrate temperature. The nature of the substrate on the other hand, apparently did not strongly influence the morphology of 50-nm thick films, which is in agreement with previous results [272]. In Fig. 4.2, three-dimensional AFM images of 50-nm thick DFH-4T films grown on top of PTAA at different deposition rates and different substrate temperatures are shown. When DFH-4T is grown at 0.2 Å/s very tall (between 300 nm and 400 nm) needle structures on top of a nice 2D layer can be observed. Increasing the substrate temperature does not really affect the height of the needles but lowers their density.

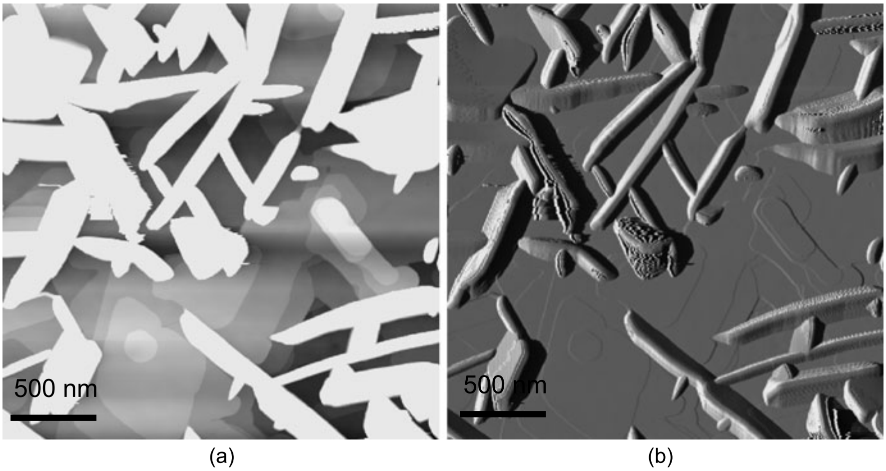

Fig. 4.1 (**a**) 2.5 μm × 2.5 μm AFM topography image of a 50-nm thick DFH-4T film grown on PTAA. A very flat 2D layer can be identified at the background. On top of this layer, large 3D needles are observed. (**b**) 2.5 μm × 2.5 μm AFM gradient image of the same layer. The 2D and 3D areas can be clearly observed. (© Wiley-VCH Verlag GmbH & Co. KGaA. Reproduced with permission)

Figure 4.2(c) and (d) show a layer of DFH-4T grown at 3 Å/s. In this case the height and the lateral size of the needles appear to be smaller. Their height is typically about 100 to 200 nm. This indicates that the transition from layered- to needle-growth can be delayed by increasing the deposition flux as well as by increasing the substrate temperature. Because a reduced height of the 3D features improves the quality and the homogeneity of the interface between the metal contact and the organic semiconductor, we typically used a deposition rate of >3 Å/s for device fabrication.

An important requirement to obtain high performance light-emitting devices is that the emitted photons are not re-absorbed by one of the other materials that is used to fabricate the device. DFH-4T is a wide-bandgap organic semiconductor, with an optical gap of 2.88 eV [273]. Thanks to its wide optical bandgap, negligible absorption is expected at the emission wavelength of DCM_2, making DFH-4T a promising candidate for use in OLEDs with field-effect electron transport. This is confirmed in Fig. 4.3, where we compare the measured normalized absorption spectrum of DFH-4T with the measured photoluminescence spectrum of Alq_3:DCM_2.

Another electron-transporting material, which has a wide band gap and therefore exhibits low absorption in the red spectral region is DFHCO-4T. The normalized absorption spectrum of DFHCO-4T, which is clearly blue-shifted with respect to the emission of DCM_2, is also shown in Fig. 4.3. In contrast to DFH-4T, its LUMO (3.9 eV) [237] is much lower than the LUMO of PTCDI-$C_{13}H_{27}$. The molecular structure of DFHCO-4T can be found in Chap. 2 (Sect. 2.1.1).

Similar to DFH-4T, AFM analysis of DFHCO-4T also reveals Stransky-Krastanov growth mode with the first few monolayers grown in a 2D arrangement

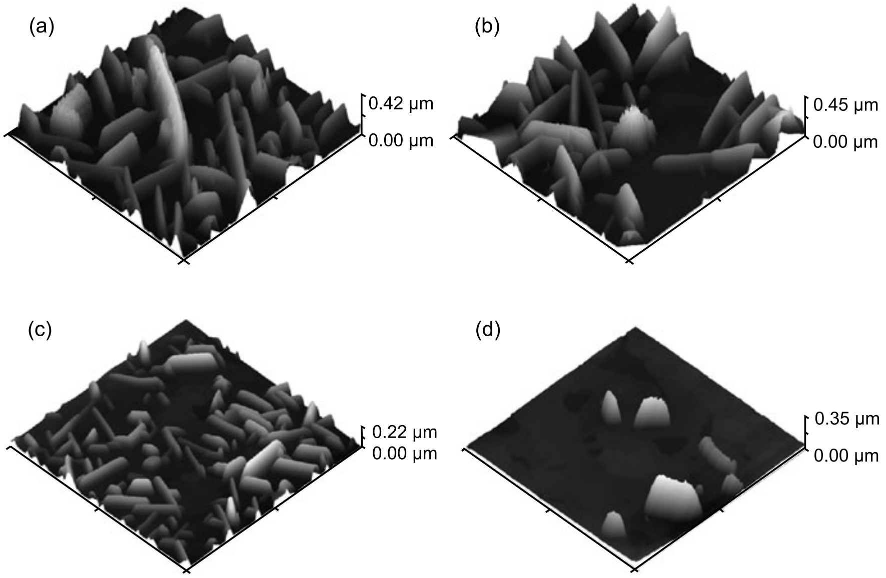

Fig. 4.2 2.5 µm × 2.5 µm three-dimensional AFM images of 50-nm thick DFH-4T films grown on top of PTAA at different deposition rates and different substrate temperatures: (**a**) flux = 0.2 Å/s and $T_{sub} = 20°C$, (**b**) flux = 0.2 Å/s and $T_{sub} = 60°C$, (**c**) flux = 3 Å/s and $T_{sub} = 20°C$, and (**d**) flux = 3 Å/s and $T_{sub} = 60°C$. (© Wiley-VCH Verlag GmbH & Co. KGaA. Reproduced with permission)

Fig. 4.3 Normalized absorption spectra of thin films of DFH-4T and DFHCO-4T and normalized photoluminescence spectrum of Alq_3:DCM_2. The low absorption in the red spectral region makes DFH-4T and DFHCO-4T particularly interesting for use in OLEDs with field-effect electron transport

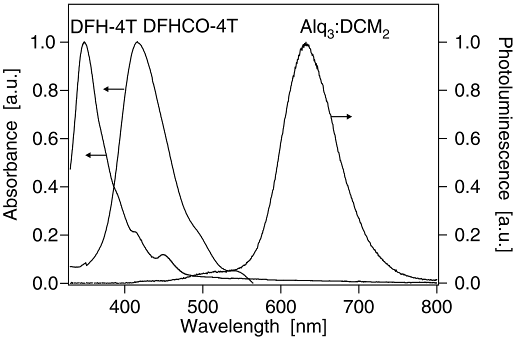

followed by a 3D lattice. Also here, the transition from 2D to 3D growth can be delayed by increasing the deposition flux as well as by increasing the substrate temperature. Figure 4.4 illustrates how the deposition conditions affect the morphology of the DFHCO-4T films. Figure 4.4(a) shows an AFM image of a 50-nm thick DFHCO-4T film grown on top of PαMS at a low deposition flux (0.2 Å/s) while the substrate was kept at room temperature. Under these conditions, a very rough morphology dominated by high peaks typical for 3D growth is observed. On the other hand, at high flux and high substrate temperature the film morphology becomes much smoother, characterized by large 2D grains with only a few 3D fea-

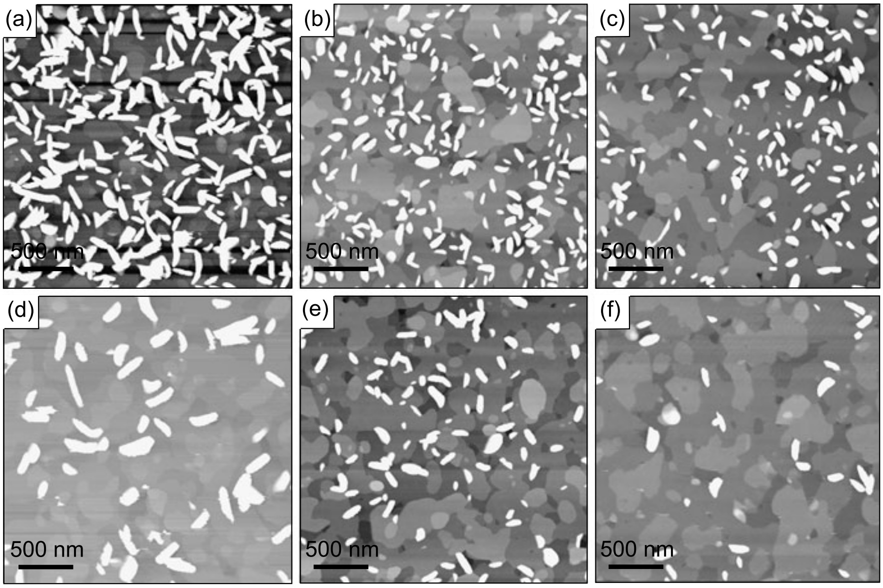

Fig. 4.4 2.5 μm × 2.5 μm AFM topography images of 50-nm thick DFHCO-4T films grown on top of PαMS at different deposition rates and different substrate temperatures: (**a**) flux = 0.2 Å/s and $T_{sub} = 20°C$, (**b**) flux = 3 Å/s and $T_{sub} = 20°C$, (**c**) flux = 4.5 Å/s and $T_{sub} = 20°C$, (**d**) flux = 0.2 Å/s and $T_{sub} = 70°C$, (**e**) flux = 3 Å/s and $T_{sub} = 70°C$, and (**f**) flux = 4.5 Å/s and $T_{sub} = 70°C$

tures (deposition rate of 4.5 Å/s and substrate temperature of 70°C, Fig. 4.4(f)). Consequently, these latter growth conditions are used for device fabrication.

4.2 Devices Based on DFH-4T

4.2.1 Transistors Based on DFH-4T

To characterize the field-effect electron transport properties of DFH-4T, we have fabricated transistors using DFH-4T as the organic semiconductor on a 100-nm thick SiO_2 dielectric. LiF/Al top contacts were used as source and drain electrodes. Prior to the deposition of DFH-4T, PTAA was spincoated. We have demonstrated earlier on that the hole-transporting wide-bandgap organic semiconductor PTAA provides a good growth surface for electron-conducting organic semiconductors, and that the hetero-interface is appropriate for electron transport. The output and transfer characteristics of these DFH-4T transistors are shown in Fig. 4.5. The effective saturation field-effect mobility for electrons at the heterojunction interface with PTAA is 0.15 cm^2/Vs. This is similar to the electron mobility we obtained for PTCDI-$C_{13}H_{27}$. We correlate this high electron field-effect mobility to the good 2D growth of the first monolayers of DFH-4T when grown on top of PTAA [274, 275].

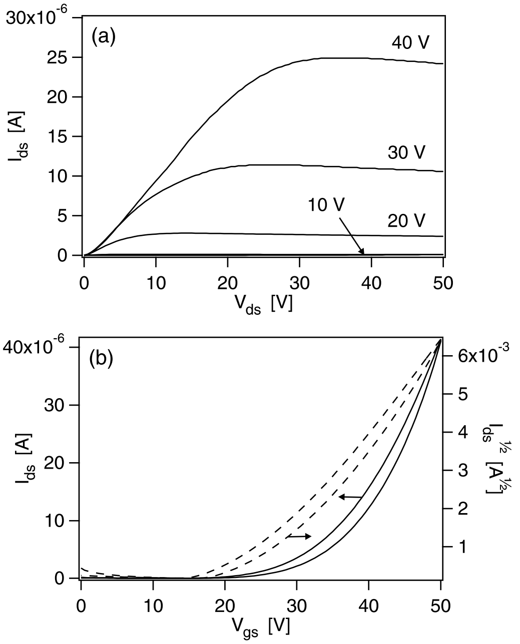

Fig. 4.5 Electrical characteristics of a DFH-4T top contact transistor ($W/L = 2000/50$): (**a**) Output characteristics, and (**b**) transfer characteristics. The saturation mobility for electrons and the threshold voltage are, respectively, 0.15 cm^2/Vs and ~24 V

To evaluate the electron transport properties of DFH-4T in OLEDs with field-effect electron transport, we also fabricated and characterized transistors using an additional Alq_3 layer in between the PTAA and the DFH-4T. Upon inserting Alq_3, the electron mobility of DFH-4T slightly dropped to a value of 0.03 cm^2/Vs.

4.2.2 DFH-4T in OLEDs with Field-Effect Electron Transport

OLEDs with field-effect electron transport comprising PTAA as the organic hole-transporting material, Alq_3:DCM_2 as the organic light-emitting layer and DFH-4T as the organic electron-transporting material have been fabricated. ITO is used as the hole-injecting electrode in the device and the cathode is formed by a thin layer of lithium fluoride (LiF) followed by deposition of aluminum (Al). Figure 4.6 displays the experimentally measured current-voltage characteristics of a device that has a width of 1 mm and where the metallic cathode was displaced by 7.2 μm with respect to the insulator edge. The measured maximum η_{ext} of the device is 0.25% (Fig. 4.13), which is more than 10 times larger than the value we obtained for devices employing 50 nm PTCDI-$C_{13}H_{27}$ as the electron-transporting material (Sect. 3.3). Clearly, this improved η_{ext}, which is approaching the efficiency of reference OLEDs with Alq_3:DCM_2 active layers [254], can be explained by the reduced absorption of the emitted photons by the electron-transporting material.

Under forward bias, the current increases with increasing voltage. However, in contrast to PTCDI-$C_{13}H_{27}$-based devices, the current appears to flatten out at volt-

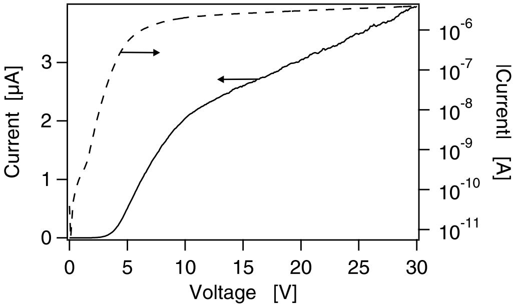

Fig. 4.6 Current-voltage characteristics of a 1 mm wide OLED with field-effect-assisted electron transport comprising the wide bandgap material DFH-4T as the electron-transporting material. The distance between the metallic top contact and the insulator edge is 7.2 µm. The *dashed line* represents the current on a logarithmic scale, whereas the *full line* is the current plotted on a linear scale. (© Wiley-VCH Verlag GmbH & Co. KGaA. Reproduced with permission)

ages exceeding 10 V. This limits the maximum current density in the device. In order to calculate the maximum electron current density, we have to consider the thickness of the accumulation layer. Since field-effect transport typically occurs in the first few monolayers of the semiconductor film [45, 276–278], we assume that the electron current flow is confined to a 6 nm thick electron accumulation layer, which corresponds to approximately two DFH-4T monolayers [272]. Taking into account this accumulation layer thickness, the maximum electron current density at 30 V is estimated to be $\sim$60 A/cm^2. This is much less than what we would expect when the current increases more or less quadratically with the applied voltage as it is the case in PTCDI-$C_{13}H_{27}$-based devices. In order to understand what limits the current increase, several control devices were measured. We fabricated devices using the organic stacks PTAA/DFH-4T and PTAA/Alq_3/DFH-4T. In both cases no flattening out of the current at higher voltages was observed. From these measurements we infer that the slower increase of the current with voltage for voltages above 10 V in Fig. 4.6 is caused by the field distribution in the device at these high voltages combined with the presence of DCM_2.

Figures 4.7(a) and (b) show the band diagrams for the device in forward bias, i.e. for a positive anode-to-cathode bias, respectively, at low and high voltages. Under these conditions electrons are injected from the cathode into DFH-4T. At low voltage bias (Fig. 4.7(a)), both the PTAA and the light-emitting layer Alq_3:DCM_2 on top of the SiO_2 are depleted of holes. The LUMO offset at the interface between Alq_3:DCM_2 and DFH-4T prohibits electron injection from DFH-4T into Alq_3:DCM_2. As a result, the depleted PTAA and Alq_3:DCM_2 layers on top of the SiO_2 insulator behave as a dielectric layer in series with the SiO_2 insulator, and an electron accumulation layer is formed in the DFH-4T at the interface with Alq_3:DCM_2. However, at higher voltage bias (Fig. 4.7(b)), the energy bands are much more bent. Since the LUMO of DFH-4T (3.3 eV) [237] is slightly higher than that of PTCDI-$C_{13}H_{27}$ (3.4 eV) [236], we assume that at high voltage bias under the influence of the electric field some electrons can overcome the energy barrier

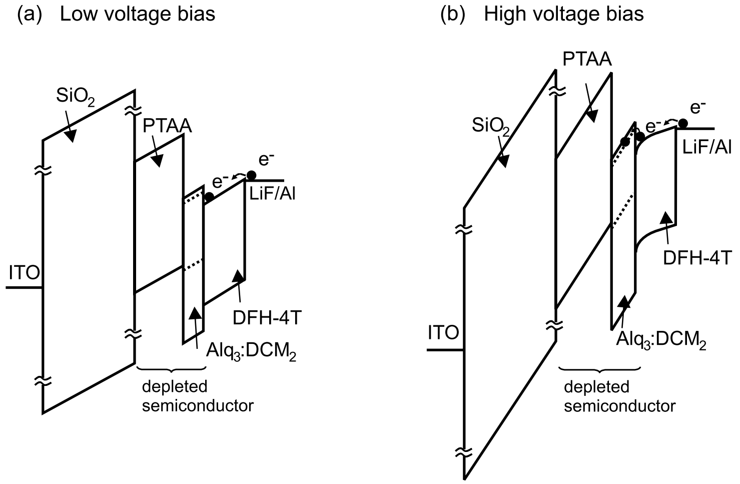

Fig. 4.7 Band diagrams for the device under forward bias conditions: (**a**) at low voltage bias, and (**b**) at high voltage bias. (© Wiley-VCH Verlag GmbH & Co. KGaA. Reproduced with permission)

and are trapped on DCM_2. This fixed charge yields, with the same field over the dielectric, less mobile charge in the channel resulting in a lower current.

This hypothesis was confirmed by measuring the characteristics of a device where a thin (10 nm) undoped layer of Alq_3 was inserted in between the Alq_3:DCM_2 light-emitting layer and the DFH-4T electron-transporting layer. In this device no flattening out of the current at high voltages was observed (Fig. 4.8) and as a result high electron current densities of 750 A/cm^2 were obtained at 30 V. η_{ext} remains unaffected upon insertion of this thin undoped Alq_3 layer (Fig. 4.13). An additional argument supporting our hypothesis is the fact that similar flattening out of the current is observed in PTCDI-$C_{13}H_{27}$-based devices when biases exceeding 40 V are applied. Since the LUMO of PTCDI-$C_{13}H_{27}$ is lower than the one of DFH-4T it is obvious that higher voltages are needed to overcome the energy barrier and to trap electrons.

4.3 Devices Based on DFHCO-4T

4.3.1 High Performance DFHCO-4T Transistors

An electron field-effect mobility of 1.7 cm^2/Vs has been reported by Yoon *et al.* for the organic semiconducting material DFHCO-4T [272]. In these devices a top-contact geometry with Au source and drain contacts was used. To check whether LiF/Al could also be used as top contact material we have fabricated DFHCO-4T transistors with LiF/Al top contacts (0.8 nm LiF followed by 100 nm Al) and compared their performance with DFHCO-4T transistors having 100 nm Au as the top

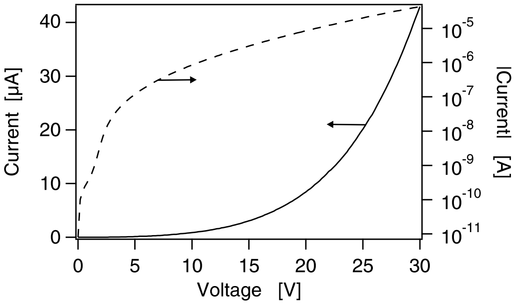

Fig. 4.8 Electrical characteristics of an OLED with field-effect-assisted electron transport comprising PTAA/Alq_3:DCM_2/Alq_3/DFH-4T as the organic layer stack. The *dashed line* represents the current on a logarithmic scale, whereas the *full line* is the current plotted on a linear scale. The device width is 1 mm and the distance between the metallic top contact and the insulator edge is 9.7 µm. (© Wiley-VCH Verlag GmbH & Co. KGaA. Reproduced with permission)

metal contact. Thin DFHCO-4T films were deposited by thermal vacuum evaporation of the material using the optimized growth conditions (Sect. 4.1). Prior to the deposition of DFHCO-4T, a 5-nm thick PαMS layer was spincoated on top of the Si/SiO_2 substrate to provide a high-quality, electron-trap free surface allowing excellent electron transport [259].

Figure 4.9(a) shows the output characteristics of a transistor with 130 µm channel length and LiF/Al top contacts. For this device, an apparent field-effect electron mobility of 0.03 cm^2/Vs was calculated. This value is more than one order of magnitude lower than the electron mobility of DFHCO-4T previously reported using Au top contacts [272]. In addition, the OTFTs show strongly non-ideal characteristics, as apparent from a superlinear dependence of the current on the drain voltage at low bias, the saturation of the output current at a more or less fixed drain-to-source bias, and a decrease of the current at higher drain voltages.

On the other hand, transistors fabricated under the same DFHCO-4T growth conditions but with Au instead of LiF/Al source-drain top contacts exhibit much better-behaved output characteristics with much higher drain currents (Fig. 4.9(b)). For Au top-contact transistors with 130 µm channel length, a mobility of 4.6 cm^2/Vs is measured. Such a remarkable mobility achieved with Au contacts is of high technological relevance because for use in complementary logic it is preferable to use a single type of source and drain metal for both the p-type and the n-type OTFTs. The reproducibility of the results is quite good. The average apparent mobility, calculated from transistors with channel lengths between 50 and 200 µm is 3.5 cm^2/Vs. These field-effect mobilities are higher compared to previously reported results [272] and we attribute this to the different growth conditions used to deposit DFHCO-4T. The fact that electrons can be efficiently injected from Au into DFHCO-4T despite an injection barrier of $\sim$1 eV is not fully understood yet. The deep LUMO (3.96 eV) [237] of DFHCO-4T and the fact that in a top-contact geometry there is a high gate-field that supports the injection of charges in a large source-gate overlap area [67] might be a possible explanation for this experimental observation.

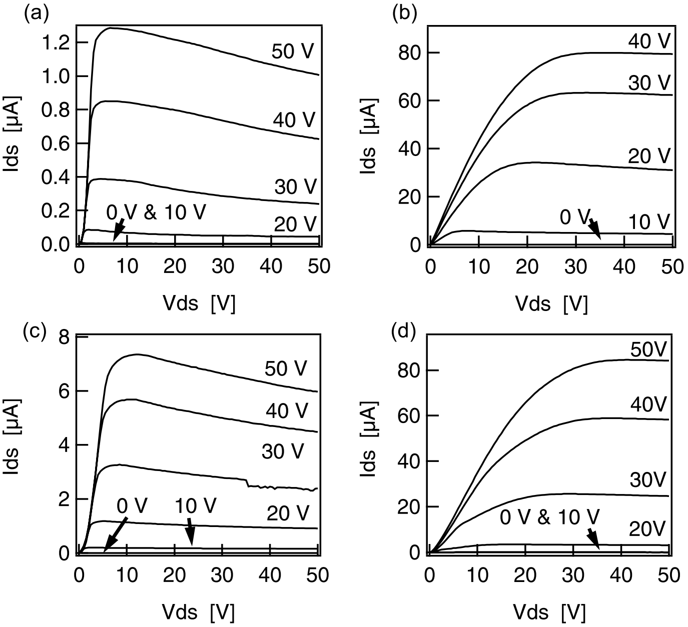

Fig. 4.9 Output characteristics of DFHCO-4T transistors ($W/L = 2000/130$) using (**a**) LiF/Al, (**b**) Au, (**c**) Yb, and (**d**) Ag top contacts. (© American Institute of Physics. Reproduced with permission)

The low apparent field-effect mobility (i.e., low output currents) and the non-ideal characteristics of DFHCO-4T transistors with LiF/Al top contacts compared to Au top contacts point to the presence of a current-limiting contact problem in the former. A plausible cause of this is the occurrence of a redox reaction between the n-type semiconductor and the Al metal contact. In fact, it is well known that ketone groups—present in the DFHCO-4T chemical structure—are easily reduced into their radical anions according to the reaction scheme shown in Fig. 4.10(a) [279]. The electron transfer reaction is driven by the oxidation of a reactive metal, as for example Mg, Al, Fe and Zn (depicted in Fig. 4.10(b) for Al) [280, 281] and the reduction of DFHCO-4T. The standard free energy ($\Delta G°$, Gibbs free energy) of the overall redox reaction depicted in Fig. 4.10(c) can be calculated by Eq. 4.1 [282], where n is the overall number of electrons exchanged between the oxidizing and reducing agents for the balanced redox equation, F the Faraday constant (96485 J/(V mol)), and $\Delta E°$ the standard cell potential (the difference in standard electrode potentials (SEPs) of both electrochemical couples). An overview of the SEPs of various oxidizing and reducing agents measured in solution is given in Fig. 4.11.

$$\Delta G° = -nF\Delta E°. \tag{4.1}$$

For the Al/Al^{3+} couple the SEP in aqueous solution is -1.662 V vs the normal hydrogen electrode (NHE) [283], which is about -1.90 V vs the reference saturated calomel electrode (SCE) [284]. Published value for the first reduction potential of

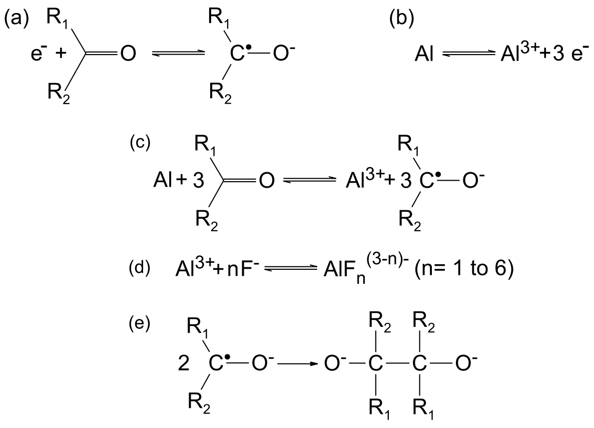

Fig. 4.10 (**a**) Reduction of a ketone, (**b**) oxidation of Al, (**c**) redox reaction between a ketone and Al, (**d**) complexation of Al^{3+} by F^-, and (**e**) dimerization of a ketone radical anion. (© American Institute of Physics. Reproduced with permission)

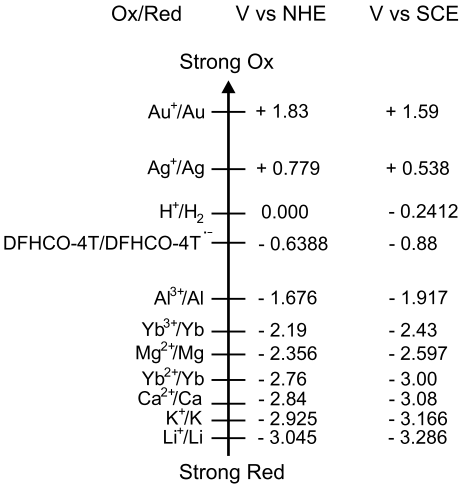

Fig. 4.11 Overview of the standard electrode potential of various electrochemical couples measured in solution

DFHCO-4T in tetrahydrofuran is -0.88 V vs the SCE [237]. Inserting this potential difference into Eq. 4.1, with $n = 3$ (Fig. 4.10(c)), gives $\Delta G° = -296$ kJ/mol. This indicates that the reaction between Al and DFHCO-4T is highly exergonic and thus thermodynamically spontaneous.

Similar reductions of organic layers by evaporation of strongly reducing metals have been reported in literature. The reaction of Al evaporated on films of Alq_3 [285–288], $F_{16}CuPc$[1] [289] and PTCDA[2] [290] for example were experimentally proven. The reduction of DFHCO-4T by evaporated Al (Fig. 4.10(c)) in our case is furthermore favored by additional side reactions. One of these reactions is the complexation of the Al^{3+} cation by fluoride ions (F^-) originating from an ultra-thin (0.8 nm) LiF layer on top of the DFHCO-4T. In fact, F^- anions are

---

[1] Copper hexadecafluorophthalocyanine.

[2] 3,4,9,10 perylenetetracarboxylic dianhydride.

well known to form stable complexes ($AlF_n^{(3-n)+}$ with $n = 1$–6, Fig. 4.10(d)) with Al^{3+} cations [291]. Furthermore, ketone radical-anions readily dimerize affording the corresponding acyloinic species (Fig. 4.10(e)) [280]. Such additional processes will enforce the DFHCO-4T/Al redox reaction (Fig. 4.10(c)) towards the right side according to Le Chatelier's principle.

The products of the reactions displayed in Fig. 4.10(c–e), an ionic salt and possibly dimerized ketone species, will form a thin interfacial layer between the unreacted DFHCO-4T and Al layers, hindering electron injection. In the case of Au this kind of reaction is impossible: the SEPs of the couples involving oxidation of Au are so high (+1.692 V vs NHE for Au/Au^+ and +1.492 V vs NHE for Au/Au^{3+}) [283] that a reaction with DFHCO-4T would be highly endergonic ($\Delta G° = +225$ kJ/mol in the case of Au/Au^+ and +619 kJ/mol for Au/Au^{3+}).

To find additional proof supporting the chemical reaction between Al and DFHCO-4T, we fabricated transistors using DFHCO-4T as the organic semiconductor but with two other top-contact metals: Ytterbium (Yb) and silver (Ag). The standard free energies for possible reactions between DFHCO-4T and Yb indicate that this kind of reaction is highly exergonic and thus spontaneous, independently if the Yb/Yb^{2+} couple (SEP: −2.76 V vs NHE [283], corresponding to $\Delta G° = -409$ kJ/mol) or Yb/Yb^{3+} couple (SEP: −2.19 V vs NHE [283], corresponding to $\Delta G° = -449$ kJ/mol) is considered. On the other hand, the corresponding value for the reaction of DFHCO-4T with Ag (SEP: +0.7796 V vs NHE [283] for Ag/Ag^+) is +139 kJ/mol, indicating that this reaction is impossible.

The output characteristics of Yb and Ag top-contact transistors with 130 μm channel length are shown in Fig. 4.9(c) and (d). Transistors with Yb top contacts show similar output characteristics and low apparent field-effect mobility (0.06 cm^2/Vs) as LiF/Al transistors, whereas Ag top-contact transistors yield much higher currents and much better-behaved output characteristics. When Ag is used as top metal contact an apparent mobility of 1.7 cm^2/Vs was measured. These results are in agreement with our argumentation and give further evidence that a redox reaction occurs at the interface between DFHCO-4T and easily oxidizable metals, similar to Hirose *et al.*'s report that PTCDA reacts with Al, but not with Au and Ag [290].

4.3.2 DFHCO-4T in OLEDs with Field-Effect Electron Transport

The high electron field-effect mobility that can be obtained in DFHCO-4T combined with the low LUMO and the low absorption in the red spectral region makes DFHCO-4T particularly interesting for use as the electron-transporting material in OLEDs with field-effect electron transport. Devices comprising PTAA as the hole-transporting layer, Alq_3:DCM_2 as the light-emitting layer and DFHCO-4T as the electron-transporting layer have been fabricated. Because DFHCO-4T only functions properly with contacts that have a low chemical reactivity such as Au and Ag, we used the inert contact metal Au to inject electrons in the device.

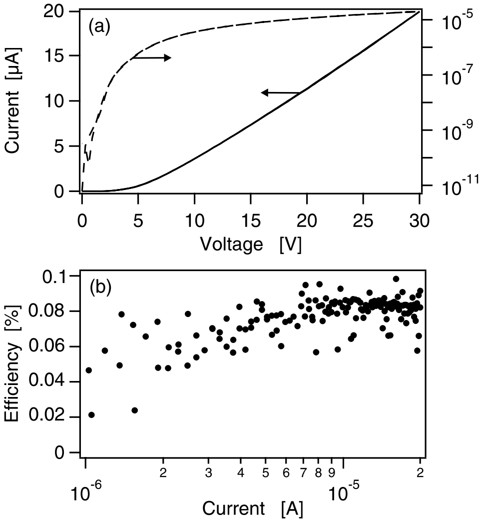

Fig. 4.12 Measured characteristics of an OLED with field-effect-assisted electron transport using the wide band gap material DFHCO-4T as the electron-transporting material. The device has a width of 1 mm and a distance between the top electrode and the insulator edge of 6.7 µm. (**a**) Current-voltage characteristics, and (**b**) η_{ext} as a function of the current

The current-voltage characteristics, the light intensity and the electroluminescence spectrum of the devices were measured. The results are summarized in Fig. 4.12. An η_{ext} of 0.08% was calculated, which is lower than the value obtained in devices using DFH-4T, but still significantly higher than the one of PTCDI-$C_{13}H_{27}$-based devices. Comparable to previous results, there is no significant reduction of η_{ext} up to the maximum current.

4.4 Comparison

An overview of the performance of different OLEDs with field-effect-assisted electron transport fabricated using various electron-transporting materials is given in Fig. 4.13. In this figure the external quantum efficiencies η_{ext} as a function of the current for devices comprising PTCDI-$C_{13}H_{27}$, DFH-4T or DFHCO-4T as the electron-transporting layer are compared. All devices presented in Fig. 4.13 have the same distance to the insulator edge (~7 µm) and were biased up to 30 V. By replacing the 50-nm thick PTCDI-$C_{13}H_{27}$ layer by DFH-4T a tenfold increase in the external quantum efficiency could be obtained. This improvement is mainly attributed to the reduced light re-absorption in the red spectral region where DCM_2 is emitting. The insertion of a thin undoped Alq_3 layer in between the DFH-4T and the active Alq_3:DCM_2 light-emitting layer does not affect this efficiency. Moreover, the presence of this undoped Alq_3 layer makes it possible to achieve high current densities in the device.

Within the error margin of about 20% we can say that PTCDI-$C_{13}H_{27}$-based devices yield a three times higher current than DFH-4T-based devices having the same displacement with respect to the insulator edge. We attribute this to the difference in mobility between PTCDI-$C_{13}H_{27}$ (0.08 cm^2/Vs) and DFH-4T (0.03 cm^2/Vs)

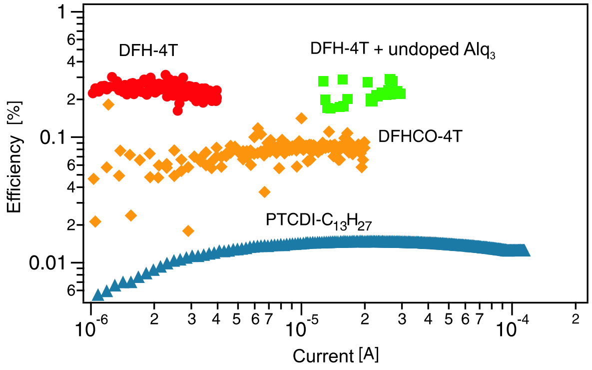

Fig. 4.13 η_{ext} as function of the current for different devices using, respectively, 50 nm of PTCDI-$C_{13}H_{27}$ (*triangles*), 50 nm of DFH-4T (*circles and squares*) or 50 nm of DFHCO-4T (*diamonds*) as the electron-transporting layer. The rectangular markers represent the η_{ext} of a device where a thin undoped Alq_3 layer is inserted in between the DFH-4T and the active light-emitting layer. All four devices have a width of 1 mm and a distance to the insulator edge of ~7 µm

when grown on top of Alq_3. On the other hand, contrary to the higher field-effect electron mobility measured in DFHCO-4T-based devices (0.8 cm^2/Vs on top of Alq_3:DCM_2), a lower current is measured. This is probably related to the very low LUMO of DFHCO-4T (3.9 eV compared to 3.3 eV for DFH-4T and 3.4 eV for PTCDI-$C_{13}H_{27}$). This low LUMO creates a large injection barrier for electrons, limiting the current through the device and prohibiting efficient recombination of holes and electrons.

4.5 Summary and Conclusions

In this chapter, two high field-effect electron-mobility organic semiconductors, DFH-4T and DFHCO-4T, were studied. Both materials have a wide band gap and show low absorption in the red spectral region. The growth of DFH-4T and DFHCO-4T was optimized and transistors using these materials as the electron-conducting semiconductor were fabricated. In addition, we compared the performance of DFHCO-4T transistors with different top-contact metals. While most n-type organic thin-film transistors show good performance when using LiF/Al as top-contact material [255, 292], we found that DFHCO-4T top-contact transistors only function properly with contacts that have a low chemical reactivity such as Au and Ag. Mobilities as high as 4.6 cm^2/Vs were demonstrated for DFHCO-4T transistors with Au top contacts, whereas the mobility of similar transistors fabricated with easily oxidizable top-contact metals, such as LiF/Al and Yb, was much lower. The reduced performance of LiF/Al and Yb top-contact transistors was attributed to an electron-transfer reaction occurring at the metal/DFHCO-4T interface. Since Au and Ag—in contrast to Al and Yb—do not react with the semiconducting material, the use of these inert metals is beneficial to achieve high-performance DFHCO-4T-based devices.

The use of DFH-4T and DFHCO-4T in OLEDs with field-effect-assisted electron transport was also investigated. Due to the reduced light re-absorption in the red spectral region where DCM_2 is emitting, higher external quantum efficiencies could be achieved compared to PTCDI-$C_{13}H_{27}$-based devices. For devices using DFH-4T as the electron-transporting material, an η_{ext} of 0.25% was demonstrated. In addition, we showed that by optimizing the growth of DFH-4T at organic hetero-interfaces, and by properly engineering the material stack of the Alq_3:DCM_2 host-guest light-emitting system to avoid carrier trapping at the guest molecules, high current densities up to 750 A/cm^2 could be achieved in the electron channel of these DFH-4T-based OLED devices. OLEDs with field-effect-assisted electron transport comprising DFHCO-4T as the electron-transporting material exhibited an η_{ext} of 0.08%. For these devices an electron current density of about 300 A/cm^2 was measured.